Asymmetric supercapacitors based on nickel decorated graphene and porous graphene electrodes

Asymmetric Supercapacitors Based on Nickel decorated Graphene and Porous Graphene Electrodes

Alberto Morenghi[1], Silvio Scaravonati[1], Giacomo Magnani[1], Michele Sidoli[1], Lucrezia Aversa[2], Roberto Verucchi[2], Giovanni Bertoni[2,3], Mauro Riccò[1], Daniele Pontiroli[1].*

1- *Nanocarbon Laboratory, INSTM& Department of Mathematical, Physical and Computer Sciences, University of Parma, Parco Area delle Scienze 7/A, 43124, Parma, Italy.*
2- *IMEM – CNR Institute of Materials for Electronics and Magnetism, Trento site c/o Fondazione Bruno Kessler, Via alla Cascata 56/C, Povo I-38123 Trento, Italy.*
3- *CNR – Istituto Nanoscienze, Via Campi 213/A, 41125, Modena, Italy.*

[*] *corresponding author email address: daniele.pontiroli@unipr.it*

Abstract:

Thermal exfoliation of graphite oxide is a scalable way to produce macroscopic amount of defective graphene-based compounds with high specific surface area, ideal as electrode materials in high-performance electrochemical supercapacitors. In order to increase the stored energy, defective graphene has been decorated with Ni nanoparticles without exposing the system to air. During the first charge cycle in an aqueous electrolyte (KOH 3.5M), Ni anchored to graphene proved to easily convert to $Ni(OH)_2$ at the nanoscale and hence to reversibly assume Ni^{2+} and Ni^{3+} valence during cyclic voltammetry, through its conversion to NiOOH. Such reversible faradaic mechanism led to a one order of magnitude increase of the specific capacitance of electrodes, reaching up to 1900 F/g at 2 mV/s in KOH 3.5M. An asymmetric supercapacitor was obtained by coupling a pure graphene negative electrode with a Ni decorated graphene positive one. The supercapacitor, operating with aqueous electrolyte, was successfully cycled in the 0-1.5 V voltage range, reaching a maximum specific energy of 37 Wh/kg and a maximum specific power of 5 kW/kg. The devices displayed good reversibility and retained 72 % of the specific energy over 10 thousand of cycles. Such promising results disclose to possible industrial implementation of graphene-based supercapacitors, for a wide range of energetic application.

Keywords: Graphene; Ni-Nanoparticles; asymmetric supercapacitors, energy storage.

1- Introduction

The global increase in energy demand drives the development of novel electrical energy storage devices, to supply higher power density and energy density than batteries [1]. Besides the unsatisfactory storage performance for several practical applications, batteries still face important issues concerning safety, limited reversibility, a few hundred cycles lifetime and serious disposal problems [2,3].

Supercapacitors (SCs) represent a promising alternative to conventional batteries. In particular, electrochemical double layer capacitors (EDLCs) store the electric energy via the fast reversible charge accumulation in the electric double layer between a highly porous electrode and an electrolyte. As in a conventional capacitor, the EDLC double layer capacitance C is given by:

$$C = \varepsilon_r \varepsilon_0 \frac{A}{d} \qquad (1)$$

where ε_r is the electrolyte dielectric constant, ε_0 is the vacuum permittivity, d is the effective thickness of the double layer, given by the size of the solvation sphere of the ions in the electrolyte and often approximated as the Debye length in aqueous electrolytes, and A is the electrode surface accessible area [4,5]. Considering the very large specific surface area (SSA) of the porous carbon electrodes (~1000 m^2/g) and a Debye length in the range of < 1 nm, the resulting specific capacitance (C_S) of an EDLC results much higher than for flat plate capacitors, of the order of hundreds F/g [5]. Nevertheless, the corresponding specific energy (E_S) accumulated in a EDLC is given by:

$$E_S = \frac{1}{2} C_S V^2 \qquad (2)$$

E_S is limited by the electrochemical window voltage (V) of the electrolyte used (usually water) and typically falls in the range 1-10 Wh/kg. Hence, EDLCs represent a much faster and reliable storage device than Li-ion batteries, although the energy they can accumulate is still far lower. For this reason, so far they have been mainly employed in conjunction with batteries, such as for energy harvesting (i.e. KERS), or in UPS and load-levelling systems, and as a replacement for batteries only in some specific cases [4].

In recent years, much research activity has been performed in order to raise SC energetic storage capacity [6–10]. For this purpose, following eq. 2, the possible identified strategies are: a) enhancing the SC capacitance and b) increasing the voltage difference between electrodes [11].

n order to improve the capacitance, electrode surface accessible to electrolyte ions can be enhanced using optimized porous carbon nanostructures. In fact, low-dimensional carbon systems have been shown to play a predominant role as energy storage materials [12–15]. In particular, graphene has attracted growing attention thanks to its high theoretical SSA (2630 m^2/g) and conductivity (~10^3 S/cm) [16]. Graphene has been largely employed as active material in electrochemical storage systems, ranging from Li and Na-ion batteries [17–23] to EDLCs, showing superior performance as compared with conventional systems [24,25].

Specific capacitance of SCs can be further increased by exploiting fast surface redox reactions occurring at the electrodes, namely pseudocapacitance and/or battery-like reactions [26–29], which can support or replace the physical charge accumulation process. In more detail, pseudocapacitance arises from two-dimensional non-diffusion limited fast and completely reversible surface redox reactions observed in some oxide materials, such as RuO_2 and MnO_2, constituting the so-called oxide supercapacitors. This process should not be confused with a battery-like "extrinsic" pseudocapacitance, emerging when a battery material is engineered at the nanoscale [30]: in such case, the power density of battery materials can be significantly increased by the decrease of the dimensions of redox-active particles [6,31]. It has been reported that graphene can efficiently support

metal oxide nanoparticles [26,29,32,33], which can provide fast and reversible faradaic effects, thus strongly enhancing the capacitance.

On the other hand, the voltage difference in SCs can be extended using non-aqueous electrolyte [25,34], which have the disadvantage of being less environment-friendly, or using an asymmetric configuration [8,9,35–38]. An asymmetric supercapacitor (ASC) consists of a battery-like faradaic electrode (as the energy source) and a capacitor-like electrode (as the power source), simultaneously offering the advantages of both supercapacitors (rate, cycle life) and advanced batteries (energy density). ASCs can make full use of the different potential windows of the two electrodes to provide a maximum operation voltage in the cell system, resulting in a greatly enhanced specific capacitance and a significantly improved energy density [36,38].

So far, various materials, such as transition metal oxides, metal hydroxides, and electronically conducting polymer materials have been extensively investigated for possible applications in ASCs. Among them, $Ni(OH)_2$ is one of the most promising candidates, thanks to its high theoretical specific capacitance (2082 F/g) and low cost [39]. Many research groups have investigated the role of $Ni(OH)_2$ directly grown on carbon-based materials, achieving good performances in term of specific energy, specific power and cyclability [35–37].

In this work, a novel asymmetric supercapacitor obtained by combining a porous graphene negative electrode with a positive electrode made of metallic nickel nanoparticle decorated graphene, operating with aqueous electrolyte (KOH 3.5 M), is presented. Graphene has been obtained via the thermal exfoliation of graphite oxide (TEGO) in inert atmosphere [17,26]. This method is easily scalable to an industrial level, making it suitable for potential applications, and allowed us to easily obtain a macroscopic amount of defective graphene with good electrical conductivity and SSA higher than 500 m^2/g. The presence of a large amount of in-plane defects and edges in TEGO sheets allowed us the anchoring of nickel (Ni) nanoparticles with an average diameter in the range 14 to 20 nm, following a well-consolidated chemical route [26].

Ni-NPs anchored in graphene matrix were then successfully electrochemically oxidized to $Ni(OH)_2$, and characterized through transmission electron microscopy, powder X-ray diffraction (PXRD) and X-ray photoelectron spectroscopy (XPS). The peculiar *in-situ* oxidation of Ni nanoparticles allowed us to evenly cover the TEGO sheets with a complex $Ni(OH)_2$ structure. This phenomenon takes place during the first oxidation semi-cycle, where a clear increase of the electrode capacitance indicates the conversion of Ni to $Ni(OH)_2$, which acts as a redox-active center. Both electrodes have been electrochemically characterized with three-electrode cyclic voltammetry (CV), showing a specific capacitance of 310(40) F/g and 1900(60) F/g at 2 mV/s for TEGO and Ni-TEGO respectively, and then assembled in an ASC. Specific energy and specific power range from 37 Wh/kg and 20 W/kg to 10 Wh/kg and 5 kW/kg, respectively. Capacitance retention (up to 72% over 10 thousand cycles at 1 A/g) and an equivalent series resistance (ESR) of 0.35(5) Ω of $Ni(OH)_2$-TEGO//TEGO ASC have been evaluated with cyclic voltammetry (CV), galvanostatic charge-discharge (GCD) cycles and electrochemical impedance spectroscopy (EIS).

2- Experimental

2.1. Materials

The synthesis of TEGO consists of graphite oxidation, followed by a thermal treatment aimed at separating the graphene layers which are stacked in the bulk graphite oxide (GO). RW-A grade graphite (SGL Carbon Group) underwent a chemical oxidation process using nitric acid and sodium chlorate to introduce functional groups with carbon-oxygen bonds on/between the graphite planes. The as-produced GO was exfoliated via thermal shock at 1150°C under high dynamic vacuum conditions. This instant heating allows the C-O groups to detach, forming a gaseous pressure of CO and CO_2, which acts as a propeller for the separation of graphite layers. This procedure is discussed in details in our previous works [17,26].

Thanks to this synthetic strategy, the obtained TEGO has unique properties such as a SSA higher than 500 m^2/g, a remarkable electronic conductivity of 9.5 S/cm and numerous active defects (dangling bonds). This defectiveness of TEGO enhances the material reactivity, promoting the anchoring of metal nanoparticles (NPs) to the surface [40]. Taking advantage of this property, we decorated TEGO with Ni-NPs following a three steps synthesis. Firstly, graphene and nickel acetylacetonate ($Ni(acac)_2$) were introduced under Argon (Ar) atmosphere in two reaction vials, then tetrahydrofuran (THF) was added to each of the vials, to suspend TEGO and to dissolve $Ni(acac)_2$. In order to obtain homogeneous solutions, the vial containing TEGO suspended in THF was magnetically stirred for 30 min; meanwhile, the vial with $Ni(acac)_2$-THF solution underwent a treatment in an ultrasonic bath. After the sonication, $Ni(acac)_2$ solution was added to the TEGO-containing vial under Ar atmosphere. In order to homogeneously blend the reagents, the mixture was magnetically stirred in a 60 °C oil bath for 12 h. Then, THF was evaporated using a liquid nitrogen condensation trap, obtaining a TEGO impregnation with $Ni(acac)_2$. The decomposition of nickel metalorganic precursor was performed through a thermal treatment at 300 °C for 30 min under high dynamic vacuum to remove the organic part of the precursor and the remaining solvent, leaving Ni-NPs electrostatically anchored to TEGO

defects [26,41]. In a previous work, TEGO decoration with Ni-NPs has been studied in depth from the point of view of synthesis conditions and Ni:C concentration, and we managed to precisely control the metal NPs dimensions [21,42]. Following this knowledge, in this work we decided to investigate the Ni:C concentration of 1:10.

2.2. Supercapacitors Assembly

The as prepared TEGO-based materials, in form of powders, were dispersed in deionized Milli-Q H_2O and ethanol solutions (1:1 in volume) through sonication. Subsequently, the dispersions were drop cast on nickel foam disks, which were previously activated through sonication in 0.1 M HCl aqueous solution. Finally, electrodes were dried in a vacuum oven at 60 °C and pressed at 50 bar pressure.

ASCs were assembled in standard coin cells (CR-2032) using glass microfiber separator (Whatman™) soaked in 3.5 M KOH aqueous electrolyte. The mass-ratio, between positive (Ni-TEGO) and negative (TEGO) electrodes, were respectively 1:8, 1:12 and 1:16 in weight of the active materials. The mass-ratio 1:8 was chosen in order to balance the charge stored in each electrode following the equation 3 [43]. The mass ratios 1:12 and 1:16 were chosen to study the behavior of the supercapacitor when electrode capacitances are not exactly matching, since a mismatch between positive and negative electrode capacitances is expected to improve the cyclability of the device [38].

$$Q_{Ni-TEGO} = Q_{TEGO} \quad \rightarrow \quad \Delta V_{Ni-TEGO} \cdot C_{Ni-TEGO} \cdot m_{Ni-TEGO} = \Delta V_{TEGO} \cdot C_{TEGO} \cdot m_{TEGO} \qquad (3)$$

2.3. Characterization Techniques

2.3.1. Electrochemical Characterization

The three-electrodes setup consists of a three-arm Swagelok cell-type, a silver-silver chloride (Ag/AgCl) reference electrode, dipped into a saturate KCl solution, a Pt wire as a counter electrode

and TEGO/Ni-TEGO coated Ni foam disks (diameter 7 mm) as working electrode. The reference electrode was separated from the cell electrolyte (KOH 3.5 M) by a glass frit. The specific capacitance of both the electrodes has been evaluated from the three-electrodes CV curves, following the equation 4, where ν is the voltage rate (mV/s), ΔV (V) is the voltage between WE and CE and I (A) is the current which flows between electrodes:

$$C_S = \frac{\int I\, dV}{\Delta V \cdot \nu} \qquad (4)$$

Two-electrodes CV was performed on ASC coin cells (CR-2032) using nickel foam disks coated with Ni-TEGO and TEGO as positive and negative electrodes, respectively. Electrochemical impedance spectroscopy (EIS) was performed with a voltage amplitude of 10 mV in the 1Hz-2MHz frequency range. CV and EIS measurements were carried out using a Keithley 2400S SourceMeter and a Gamry Instrument 1010E Interface Potentiostat. The data collection and analysis were performed with Mathworks Matlab® software. Galvanostatic charge-discharge cycles were carried out with a Neware BTS4000-5V50mA Battery Testing System with a specific current (I_s) ranging from 20mA/g to 10 A/g, calculated from the current supplied (I) and the average mass (m_A), equivalent to the half of the electrodes total mass, as follow:

$$I_s = \frac{I}{m_A} = \frac{I}{m_T/2} \qquad (5)$$

[35]

From charge-discharge cycles at different current rates, the specific energy and power were calculated as follow:

$$E_S = \frac{\int_{t_1}^{t_2} I\, V\, dt}{3600\, m_T} \qquad (6)$$

$$P_S = \frac{E_S \cdot 3600}{\Delta t} \qquad (7)$$

Where $\Delta t = t_2 - t_1$ is the time interval of discharging process, the numerical factor (3600) is due to the conversion from *J* to *Wh* and m_T is the total mass of active materials. The energy retention was evaluated over 10 thousand of charge-discharge cycles with a specific current of 1 A/g.

2.3.2. Structure and Morphological Characterization

The structure and chemical composition of Ni-TEGO electrodes were studied, before and after the electrochemical characterization, by means of powder X-ray diffraction (PXRD) with a Bruker D8 Discover diffractometer operating in Debye Scherrer geometry, equipped with copper anode (Cu-Kα) and a Rayonix MX225 2D area detector. The data were analyzed with Fit2D and GSAS-II software. To evaluate the chemical state of Ni, X-ray photoelectron spectroscopy (XPS) has been carried out in an ultra-high-vacuum (UHV) system [44], equipped with a non-monochromatized X-ray source (Mg Kα photon at 1253.6 eV) and a VSW HA100 hemispherical analyzer (with PSP electronic power supply and control), leading to a total energy resolution of 0.86 eV. The binding energy (BE) scale of XPS spectra was calibrated by using the Au 4f peak at 84.0 eV as a reference. The core level analysis has been performed by Voigt line-shape deconvolution after background subtraction of a Shirley function. The morphology of the Ni-TEGO samples was observed through high resolution transmission electron microscopy (HRTEM) and scanning transmission electron microscopy (STEM) performed with a JEOL JEM-2200FS working at 200 kV and equipped with annular dark-field (ADF) detectors, before and after the electrochemical characterization in the 3-electrode CV. The samples were dispersed in ethanol and a droplet was deposited on Cu grids with lacey carbon support films. Chemical quantification was performed with energy dispersive X-ray spectroscopy (EDS) using a silicon-drift detector (SDD). The oxidation state of Ni was verified from the Ni-$L_{2,3}$ edge shape acquired with electron energy-loss spectroscopy (EELS) using an in-column filter.

3- Results and Discussion

3.1 Materials Characterization

3.1.1 Three-Electrodes Cyclic Voltammetry

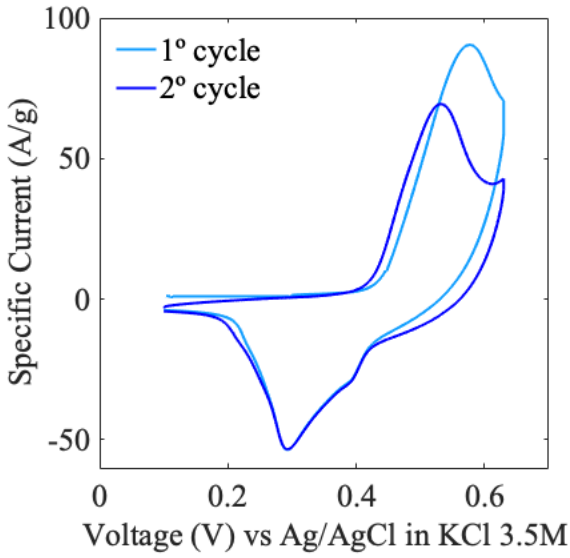

Figure 1. Three-electrode cyclic voltammetry of Ni-TEGO electrode at $\nu = 20\,mV/s$. Oxidation of metallic nickel nanoparticles into nickel hydroxide is evident during the first oxidation peak of the first cycle.

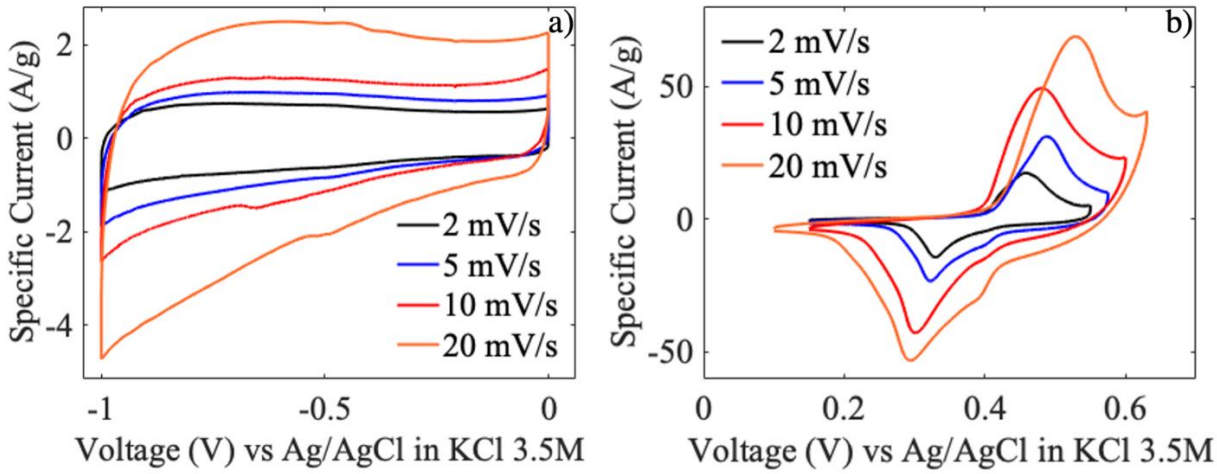

Figure 2. Three-electrodes cyclic voltammetry of TEGO (a) and Ni-TEGO (b), performed at 2 mV/s, 5 mV/s, 10 mV/s and 20 mV/s voltage rates.

Three-electrodes CV was performed on both Ni-TEGO and TEGO electrodes at different rates (range 2 mV/s - 200 mV/s). During the first oxidation semi-cycle, the Ni-TEGO electrode underwent an irreversible oxidation reaction where Ni-NPs converted to $Ni(OH)_2$, as shown in Figure 1. This process is depicted by the decrease of the CV curve enclosed area and by the clear shift of the oxidation peak from 0.58 V to 0.52 V in the two subsequent cycles performed at $\nu = 20$ mV/s. Three-electrodes CV of TEGO and Ni-TEGO are shown in Figure 2. TEGO shows a typical capacitive behavior with a quasi-rectangular shape from 2 mV/s to 200 mV/s, with no clear evidence of redox peaks. The position of reduction and oxidation peaks in Figure 2b at 0.33 V and 0.45 V respectively (CV at $\nu = 2$ mV/s) are associated with the reduction and oxidation of the $Ni(OH)_2$ – NiOOH redox active couple [45] with respect to the Ag/AgCl reference electrode. The specific capacitance of the electrodes, evaluated from the three-electrodes CV with equation 4 as a function of ν, are shown in Table 1. These values (calculated at $\nu = 10\ \mathrm{mV/s}$) were used for the calculation of the mass-ratios of asymmetric SC electrodes following equation 3.

Table 1. Specific capacitance of Ni-TEGO and TEGO -based electrodes, calculated with three-electrodes CV as a function of ν.

		2 mV/s	*5 mV/s*	*10 mV/s*	*20 mV/s*	*50 mV/s*
Specific Charge (F/g)	Ni-TEGO	1900(60)	1333(50)	1280(40)	840(25)	680(20)
	TEGO	310(40)	165(20)	110(15)	100(13)	95(12)

3.1.2 X-Ray Diffraction

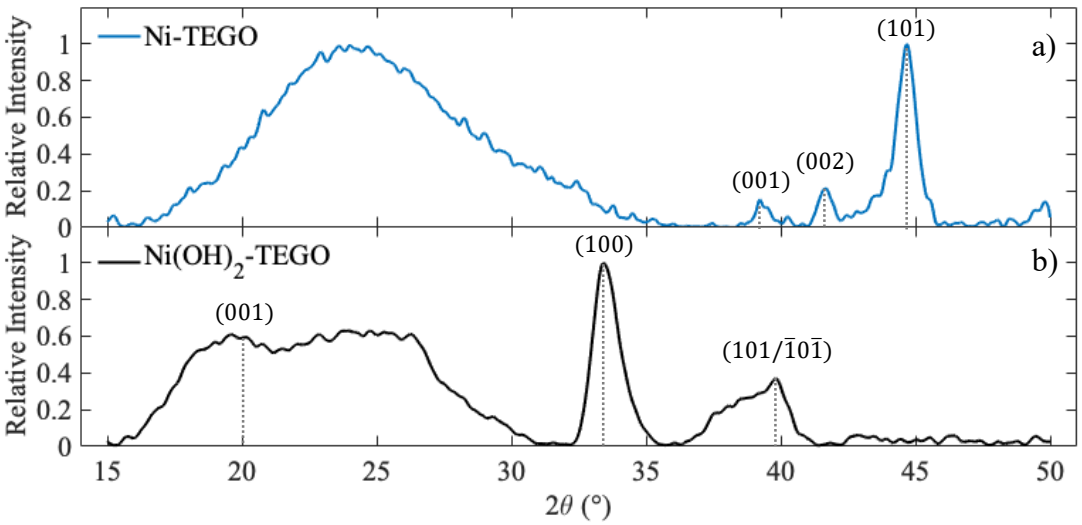

Figure 3. Diffraction patterns of Ni-TEGO sample before (a) and after (b) the oxidation in the electrochemical cell. After the oxidation, metallic nickel nanoparticles oxidize into nickel hydroxide.

PXRD was performed both on pristine and oxidized positive electrode (Figure 3). The diffraction patterns show the transformation of the metallic Ni-NPs into nickel hydroxide after the electrochemical reaction. Both the diffraction patterns exhibit a broad band around $2\theta = 24°$ arising from the (002) reflection of few-layers graphene nanocrystals [46]. Specifically, in Figure 3a, Ni peaks at $2\theta = 39.3°, 42.6°$ and $44.5°$ are associated to the (100), (002) and (101) plane reflections of hexagonal $P6_3/mmc$ structure of pure Ni [47] (a = 2.64 Å, c = 4.34 Å), respectively. The cell parameters were optimized with the Rietveld refinement method. It is worth noting that the difference of the intensity of the main experimental peak with the calculated one suggests that a further cubic fcc Ni phase could be present in the sample, which has its main peak at $2\theta = 44.6°$. Therefore, the asymmetric broadening of the (101) peak could be associated with the presence of stacking faults and strains, due to the transition from the hexagonal close packed (hcp) structure to the fcc one. The analysis of the Ni peaks broadening with the Scherrer equation returns a 14(5) nm mean diameter for

the Ni-NPs, according to our previous analysis [26]. The diffraction pattern of Ni-TEGO sample, collected after oxidation, is shown in Figure 3b and matches with the hexagonal P-3ml crystallographic structure (a = 3.1 Å, c = 4.2 Å) of $Ni(OH)_2$ [48]. Specifically, three peaks are distinguishable at $2\theta = 21°, 33°$ and $40°$ associated with the (001), (100) and (101)/(-10-1) reflections of the $Ni(OH)_2$ hexagonal structure.

3.1.3 X-Ray Photoelectron Spectroscopy

XPS analysis performed on $Ni(OH)_2$-TEGO electrode, which was obtained through the Ni-TEGO oxidation in 6 CV cycles, revealed the presence of carbon (C1s core level), oxygen (O1s), nickel (Ni2p), and sodium (Na1s) with atomic percentages of 74.02%, 21.43%, 4.17%, and 0.38%, respectively. C1s core level (see Fig. 4, left) has a main component located at 284.48 eV due to sp^2 carbon atoms, showing asymmetry typical of few layers graphene [49,50]. The peak at 285.30 eV is related to sp^3 carbon atoms, and it is evidence of defects in the layered graphene structure [50]. Other features are located at 286.75, 288.26, and 289.60 eV and are due to C-O, C=O, and C=OR species (see Tab. S1 for further details) [51]. O1s core level reflects the presence of all these carbon-oxygen based chemical groups (see Fig. S1 and Tab. S1) [52]. A weak component at high BE (534.96 eV) can be attributed to water, while the main peak at 531.24 eV is due to chemical bonds with nickel. Ni2p core level shows two main bands (see Fig.S2) due to spin-orbit splitting, Ni2p 3/2 located at about 856.3 eV and Ni2p 1/2 at about 874.0 eV. The deconvolution of Ni2p 3/2 peak is based on previous studies [53–55] and the use of a Shirley background applied across the entire Ni2p spectrum with an offset in the high BEs region [56], as shown in Fig. S2. The Ni2p 3/2 core level can be properly fitted using a six components multiplet structure that is typical of $Ni(OH)_2$ metal hydroxide [53,54]. The first peak BE is 855.71 eV, while the other components have BEs and intensity according to the proposed model for $Ni(OH)_2$ multiplet structure [53,54]. The experimental BE has a +0.8 eV shift to the theoretical value, but this kind of variability has often been observed for transition metal oxides [45,53,57,58]. Accordingly, a similar shift (+0.4 eV) is also present for O1s component related

to oxygen bond with nickel (see Fig. S1 and Tab. S1). Any presence of NiO, Ni^{+3}, or Ni^{0} components would profoundly change the overall Ni2p core level lineshape that definitely, evidences the presence of the Ni^{2+} hydroxide only [54,56].

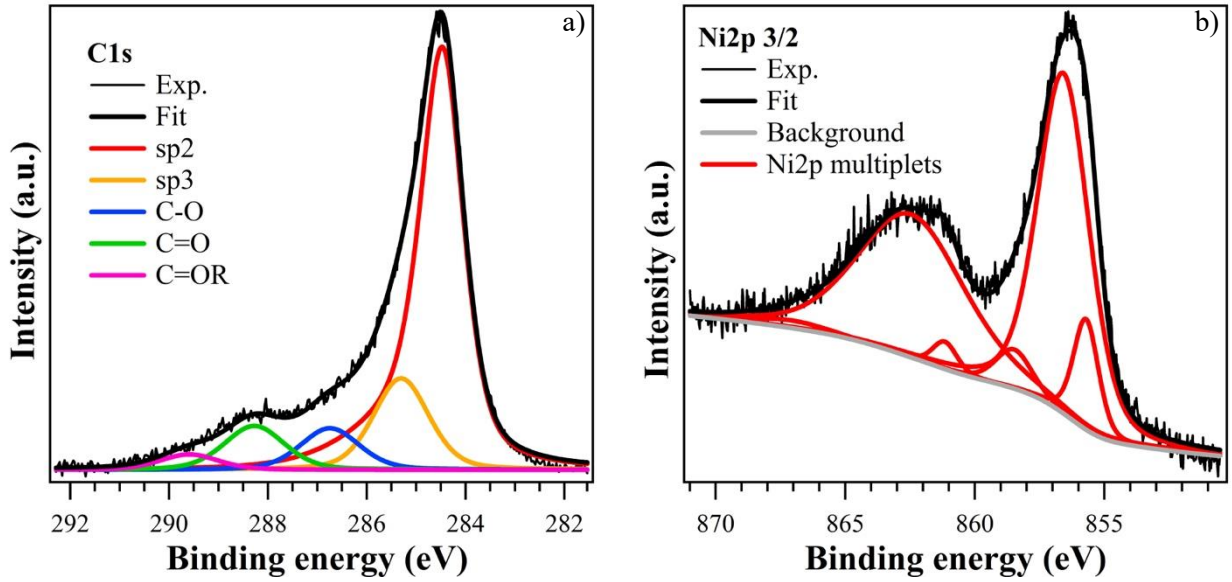

Fig. 4. XPS analysis of C1s (a) and Ni2p 3/2 (b) core levels for $Ni(OH)_2$-TEGO. C1s spectrum is background subtracted. Main components are shown.

3.1.4 High-resolution Electron Microscopy

Ni-NPs, anchored to TEGO defects, were observed to have an average diameter of 20(9) nm, estimated from the size distribution of about 500 particles as measured in STEM experiment (see Figure S5). This result is in according to our previous analysis [26] and is consistent with the Scherrer analysis of X-ray diffraction pattern. TEM images of Ni-TEGO, before and after the oxidation, are shown in Figure 5. The metallic Ni-NPs, anchored to the TEGO defects (a), through the conversion into nickel hydroxide, evolves from a sparse distribution of rounded nanoparticles into a complexed $Ni(OH)_2$ coverage of the TEGO films (b). In fig. 5 c) it is shown a Ni nanoparticle on TEGO sheet with fringes corresponding to (101) planes with $d_{Ni(101)}$ = 0.20 nm as in the hcp Ni structure. These planes are also indicated for clarity in the diffractogram in the inset of Figure 5 c). In Figure 5 d) it is shown the sample after the electrochemical treatment with a distributed oxidized Ni with small

domains (darker regions in the image) on TEGO. Unfortunately, it is hard to address the structure of such very small domains with HRTEM, due to fast evolution in NiO under the 200 kV electron beam. The diffractogram in Figure 5 d) shows a faint broad ring corresponding to (001) planes from $Ni(OH)_2$ ($d_{Ni(OH)2(001)}$ = 0.46 nm) while emerging reflections from (111) and (200) NiO planes already visible. Figure 5 e) and f) show the spectra of nickel NP and of nickel hydroxide, respectively. The Ni-L edge shows a very different shape between the pristine Ni-TEGO sample (e) and the treated sample. The black lines in the EEL spectra mark the continuum of states (from an Hartree-Slater model) used to isolate the contribution of the *d*-states (white-lines) in the spectra. The latter were used to calculate the white-line ratio L_3/L_2 and derive the valence state, according to the procedure of Graetz et al. [59]. The valence resulted +0.6(0.2) for the pristine sample and +1.8(0.2) after oxidation, confirming the XPS results. The very small oxidation in the pristine sample may derive from the exposure to air before entering the microscope.

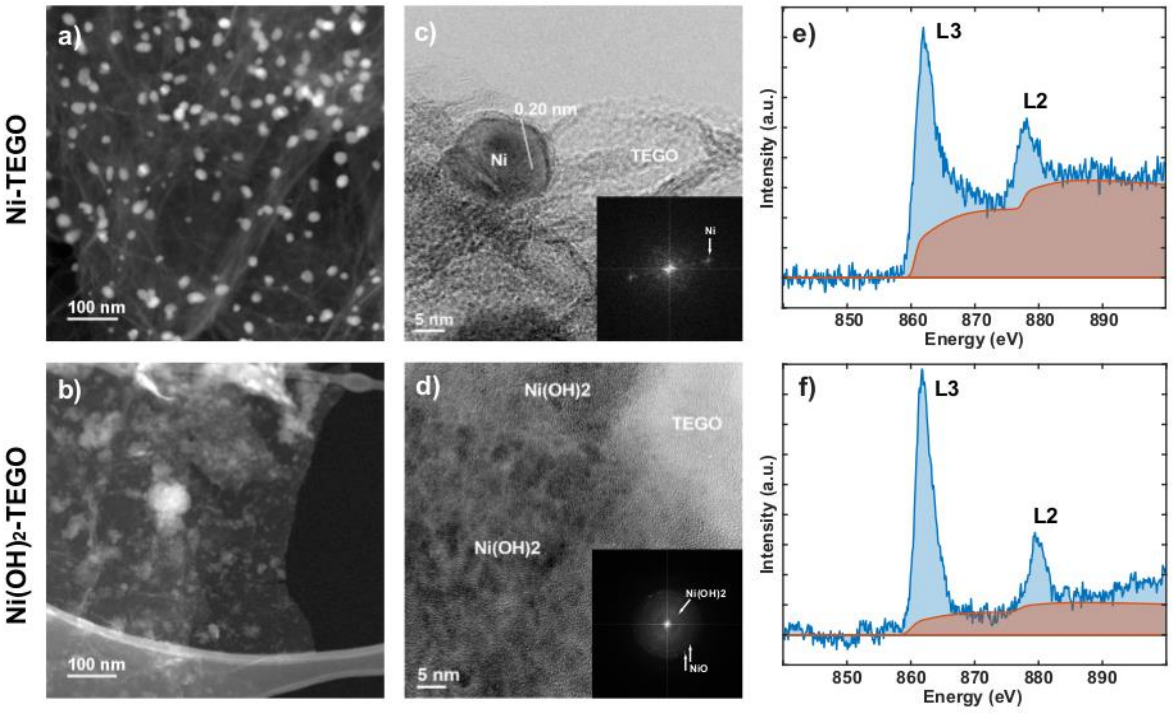

Figure 5. Comparison of the pristine Ni-TEGO sample and the Ni(OH)2-TEGO sample after treatment. (a, b) ADF-STEM images from the pristine sample and the sample after treatment. (c) HRTEM image of a Ni nanoparticle in the pristine Ni-TEGO sample. d) HRTEM image after treatment of the Ni-TEGO sample. (e, f) EELS spectra of Ni-TEGO before and after the oxidation.

3.2 Asymmetric Supercapacitor Characterization

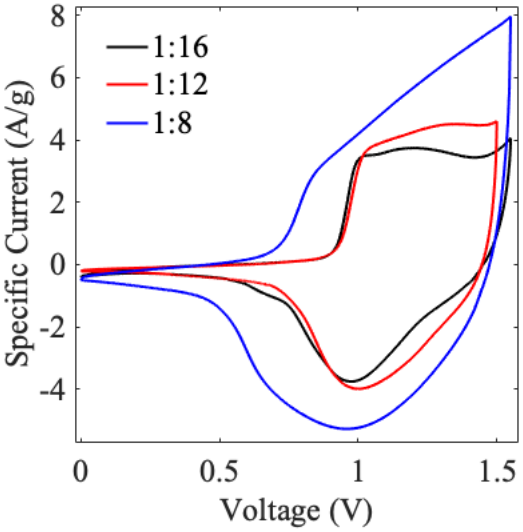

Figure 6. Comparison of the two-electrodes CV curves, collected at $\nu = 20$ mV/s, of ASCs with different mass-ratio between positive and negative electrodes.

3.2.1 Two-Electrodes Cyclic Voltammetry

The two-electrodes CV of all the three ASCs with different mass ratio of positive and negative electrodes showed an improved working voltage window up to 1.5 V. The 1:12 and the 1:16 mass ratio SCs showed CV shapes almost flat from 1 V to almost 1.5 V (see Figure S6), while the 1:8 SC exhibited a smoother CV profile (See Figure 6). On the other hand, the choice of the 1:8 mass ratio allowed to optimize the capacitance of the device, associated with the area enclosed into the CV curve, which reached 70(3) F/g at $\nu = 5$ mV/s, while 1:12 and 1:16 ASCs reached both 37(1) F/g at $\nu = 5$ mV/s. In Fig. 7 a) and b) it is shown the behavior of the 1:8 mass-ratio ASC as a function of ν. The shape of the voltammetric curve is maintained up to $\nu = 500$ mV/s.

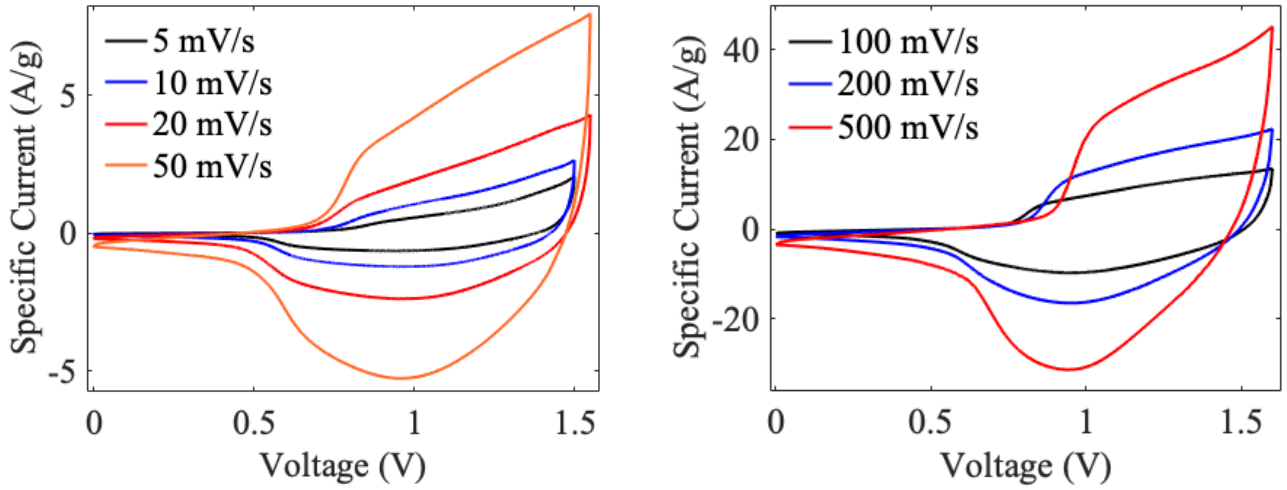

Figure 7. Two-electrodes cyclic voltammetry of 1:8 mass-ratio ASCs as a function of the rate.

3.2.3 Galvanostatic Charge-Discharge Cycles

The GCD cycles of 1:8 mass-ratio ASC performed at different specific currents are shown in the insets of Figure 8. The cycle shape, maintained also at high specific currents, shows the typical behavior of a hybrid capacitor. Specifically, the galvanostatic cycles, performed between 0 V to 1.5 V, display the presence of plateaus associated with the occurrence of $Ni(OH)_2$ faradaic reactions. The peculiar shape is maintained also at very high specific current, with no increase of the equivalent series resistance (ESR), which was evaluated as 0.35(5) Ω by means of EIS. The capacitance retention (see Figure 8) was then evaluated through 10000 cycles at the specific current of 1 A/g. The performance of the device falls to 74% of the initial capacitance during the first 2000 galvanostatic cycles, then it remains almost stable, reaching the 72% of the initial capacitance after 10000 cycles. The galvanostatic cycles performed at different specific currents enabled us to evaluate the specific energy and the specific power with equations 5 and 6, respectively. These values are shown in a Ragone Plot in Fig. 9 and were compared to other literature ASCs data [60,61].

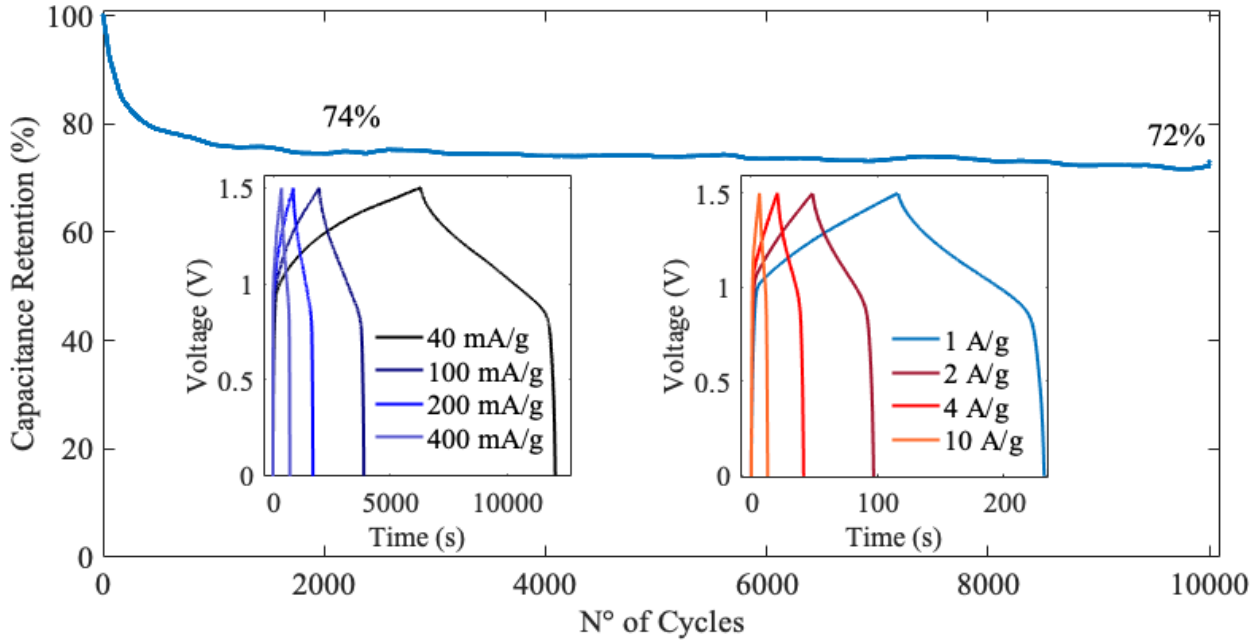

Figure 8. Capacitance retention over 10000 galvanostatic cycles of charge discharge at 1 A/g. Inset: galvanostatic cycles performed from low (40 mA/g) to high specific currents (10 A/g).

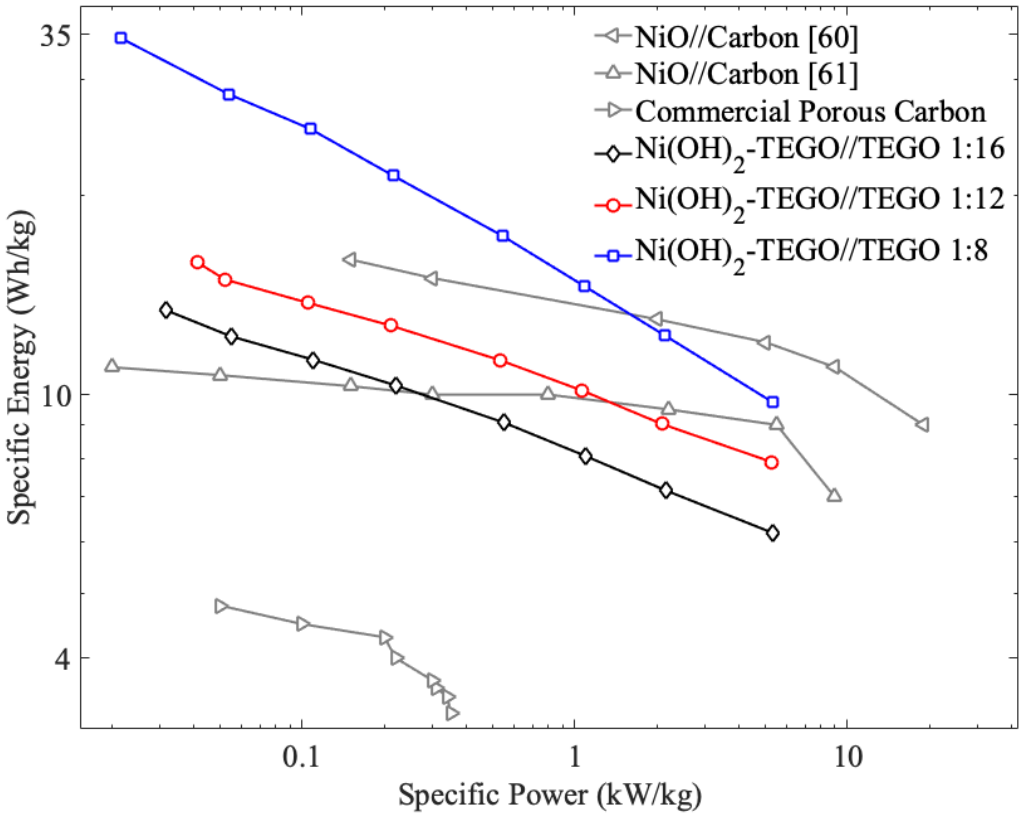

Figure 9. Comparison in a Ragone Plot of the three asymmetric supercapacitors with $Ni(OH)_2$-TEGO positive electrodes ($Ni(OH)_2$-TEGO : TEGO = 1:8, 1:12 and 1:16) with literature asymmetric supercapacitors based on NiO//Carbon [60] [61] and commercial porous carbon-based supercapacitors.

3.2.4 Discussion

In this work, the assembly of an asymmetric SC has been obtained by coupling two graphene-based different electrodes: one, operating as a negative electrode, exploited defective graphene obtained via the thermal exfoliation of graphite oxide as an active material, supported on Ni foam. Thanks to the peculiar and scalable synthesis process, TEGO shows high porosity, good electrical conductivity and can be produced in large amount. The other, operating as a positive electrode, consisted in a hybrid system, where the same defective graphene was previously decorated with almost monodispersed Ni nanoparticles, with average diameter of about 20(9) nm. Through an irreversible electrochemical process, which can take place directly in the newly assembled devices, Ni nanoparticles easily convert

to $Ni(OH)_2$ by reacting with the OH^- species of the base electrolyte (KOH 3.5 M). It is worth noting that the oxidation of Ni-NPs into $Ni(OH)_2$ does not deplete the electrolyte from OH^- species, since the estimated number of dispersed OH^- ions exceeds of about three orders of magnitude that of nickel atoms decorating the electrode. After the reaction, a profound change of the morphology occurs, as the small Ni nanoparticles are replaced by a complex $Ni(OH)_2$ coverage of the graphene sheets, as shown by electron microscopy. Such morphological arrangement in this $Ni(OH)_2$-graphene composite is rather unusual, if compared with literature; in that case, in fact, the Ni oxide or hydroxide source of redox reactions is usually obtained by means of hydrothermal synthesis, leading to the typical formation of Ni hydroxide nanostructures, such as flower or nanoplatelets [32,35], or by direct electrochemical deposition of Ni or Ni hydroxide on the carbon matrix [62]. Thanks to our peculiar synthesis strategy, the Ni-TEGO electrode displayed an specific capacitance of 1900 F/g at 2 mV/s rate, higher than most of literature reported values [36,39,63,64]. Moreover, when the rate is increased to 50 mV/s the electrode retained about 700 F/g. Probably, such large values are due to the synergistic effect between TEGO and $Ni(OH)_2$ nanostructures which, covering the TEGO sheets, are expected to reach comparable SSA. The complete ASCs, operating with aqueous electrolyte in an extended voltage window, delivered a very good energy density and high rate capability. Also, the capacitance retention of the optimized device, evaluated over 10000 galvanostatic cycles, after an initial drop observed in the first 2000 cycles, possibly due to an irreversible evolution of the hybrid electrode which is still not completely understood, remained almost stable over the remaining 8000 cycles, suggesting a superior cycling stability of these ASCs.

4- Conclusions

We have successfully developed an asymmetric supercapacitor using our thermally exfoliated graphene oxide (TEGO) and nickel decorated TEGO as negative and positive electrodes, respectively. TEGO has a high specific surface area of more than 500 m^2/g and its scalable synthesis does not

involve the use of heavy metals. Metal Ni nanoparticles, with an average diameter of 20(9) nm, undergoes an in-site oxidation evolving to a complexed $Ni(OH)_2$ coverage of the TEGO during the early cycles of the electrode, which reaches a remarkable specific capacitance of 1900 F/g at 2 mV/s. The ASC was tested through cyclic voltammetry revealing an extended working voltage window of about 1.5 V with an aqueous electrolyte and through galvanostatic charge-discharge cycles reaching a maximum specific energy of 37 Wh/kg at 40 mA/g and 10 Wh/kg at 10 A/g. The device was tested over 10000 galvanostatic cycles revealing that the after the first 2000 cycles the capacitance remains almost stable, with the device which keeps 72% of the initial capacitance over the successive 8000 galvanostatic cycles. These findings disclose to novel possible applications of scalable graphene-based asymmetric supercapacitors in fields where high power and high energy are required.

Acknowledgements

The authors acknowledge financial support from the Cariplo Foundation (project number 2019-2152, 'Gaining health and energy from Lombard agrifood waste').

References

[1] B.E. Conway, Electrochemical supercapacitors: scientific fundamentals and technological applications, Springer Science & Business Media, 2013.

[2] C. Arbizzani, G. Gabrielli, M. Mastragostino, Thermal stability and flammability of electrolytes for lithium-ion batteries, J. Power Sources. 196 (2011) 4801–4805.

[3] B. Huang, Z. Pan, X. Su, L. An, Recycling of lithium-ion batteries: Recent advances and perspectives, J. Power Sources. 399 (2018) 274–286.

[4] P. Simon, Y. Gogotsi, Materials for electrochemical capacitors, in: Nanosci. Technol. a Collect. Rev. from Nat. Journals, World Scientific, 2010: pp. 320–329.

[5] F. Béguin, V. Presser, A. Balducci, E. Frackowiak, Carbons and electrolytes for advanced supercapacitors, Adv. Mater. 26 (2014) 2219–2251.

[6] V.I. Birss, B.E. Conway, J. Wojtowicz, The role and utilization of pseudocapacitance for energy storage by supercapacitors, (1997).

[7] Y. Zhu, S. Murali, M.D. Stoller, K.J. Ganesh, W. Cai, P.J. Ferreira, A. Pirkle, R.M. Wallace, K.A. Cychosz, M. Thommes, Carbon-based supercapacitors produced by activation of graphene, Science (80-.). 332 (2011) 1537–1541.

[8] M. Rajkumar, C.-T. Hsu, T.-H. Wu, M.-G. Chen, C.-C. Hu, Advanced materials for aqueous supercapacitors in the asymmetric design, Prog. Nat. Sci. Mater. Int. 25 (2015) 527–544.

[9] W.G. Pell, B.E. Conway, Peculiarities and requirements of asymmetric capacitor devices based on combination of capacitor and battery-type electrodes, J. Power Sources. 136 (2004) 334–345.

[10] D. Pontiroli, S. Scaravonati, G. Magnani, L. Fornasini, D. Bersani, G. Bertoni, C. Milanese, A. Girella, F. Ridi, R. Verucchi, Super-activated biochar from poultry litter for high-performance supercapacitors, Microporous Mesoporous Mater. 285 (2019) 161–169.

[11] J. Yan, Q. Wang, T. Wei, Z. Fan, Recent advances in design and fabrication of electrochemical supercapacitors with high energy densities, Adv. Energy Mater. 4 (2014) 1300816.

[12] L. Sun, X. Wang, Y. Wang, Q. Zhang, Roles of carbon nanotubes in novel energy storage devices, Carbon N. Y. 122 (2017) 462–474.

[13] M. Gaboardi, C. Milanese, G. Magnani, A. Girella, D. Pontiroli, P. Cofrancesco, A. Marini, M. Riccò, Optimal hydrogen storage in sodium substituted lithium fullerides, Phys. Chem. Chem. Phys. 19 (2017) 21980–21986.

[14] G.X. Wang, J.H. Ahn, J. Yao, M. Lindsay, H.K. Liu, S.X. Dou, Preparation and characterization of carbon nanotubes for energy storage, J. Power Sources. 119–121 (2003) 16–23.

[15] D. Pontiroli, D. D'Alessio, M. Gaboardi, G. Magnani, C. Milanese, S. G. Duyker, V. K. Peterson, N. Sharma, M. Riccò, Ammonia-storage in lithium intercalated fullerides, J. Mater. Chem. A. 3 (2015) 21099–21105.

[16] R. Raccichini, A. Varzi, S. Passerini, B. Scrosati, The role of graphene for electrochemical energy storage, Nat. Mater. 14 (2015) 271–279.

[17] J.C. Pramudita, D. Pontiroli, G. Magnani, M. Gaboardi, M. Riccò, C. Milanese, H.E.A. Brand, N. Sharma, Graphene and Selected Derivatives as Negative Electrodes in Sodium-and Lithium-Ion Batteries, ChemElectroChem. 2 (2015) 600–610.

[18] J. Hassoun, F. Bonaccorso, M. Agostini, M. Angelucci, M.G. Betti, R. Cingolani, M. Gemmi, C. Mariani, S. Panero, V. Pellegrini, B. Scrosati, An Advanced Lithium-Ion Battery Based on a Graphene Anode and a Lithium Iron Phosphate Cathode, Nano Lett. 14 (2014) 4901–4906.

[19] P. Lian, X. Zhu, S. Liang, Z. Li, W. Yang, H. Wang, Large reversible capacity of high quality graphene sheets as an anode material for lithium-ion batteries, Electrochim. Acta. 55 (2010) 3909–3914.

[20] J.C. Pramudita, A. Rawal, M. Choucair, D. Pontiroli, G. Magnani, M. Gaboardi, M. Riccò, N. Sharma, Mechanisms of Sodium Insertion/Extraction on the Surface of Defective Graphenes, ACS Appl. Mater. Interfaces. 9 (2016) 431–438.

[21] J.C. Pramudita, D. Pontiroli, G. Magnani, M. Gaboardi, C. Milanese, G. Bertoni, N. Sharma, M. Riccò, Effect of Ni-nanoparticles decoration on graphene to enable high capacity sodium-ion battery negative electrodes, Electrochim. Acta. 250 (2017) 212–218.

[22] C. Arbizzani, L. Da Col, F. De Giorgio, M. Mastragostino, F. Soavi, The Role of Modified Graphene in Cathode Formulations for Lithium-Ion Batteries, ECS Trans. 66 (2015) 139.

[23] C. Arbizzani, L. Da Col, F. De Giorgio, M. Mastragostino, F. Soavi, Reduced Graphene Oxide in Cathode Formulations Based on LiNi0.5Mn1.5O4, J. Electrochem. Soc. 162 (2015) A2174.

[24] L.L. Zhang, R. Zhou, X.S. Zhao, Graphene-based materials as supercapacitor electrodes, J. Mater. Chem. 20 (2010) 5983–5992.

[25] S.R.C. Vivekchand, C.S. Rout, K.S. Subrahmanyam, A. Govindaraj, C.N.R. Rao, Graphene-based electrochemical supercapacitors, J. Chem. Sci. 120 (2008) 9–13.

[26] M. Gaboardi, A. Bliersbach, G. Bertoni, M. Aramini, G. Vlahopoulou, D. Pontiroli, P. Mauron, G. Magnani, G. Salviati, A. Züttel, Decoration of graphene with nickel nanoparticles: study of the interaction with hydrogen, J. Mater. Chem. A. 2 (2014) 1039–1046.

[27] R. Della Noce, S. Eugénio, M. Boudard, L. Rapenne, T.M. Silva, M.J. Carmezim, S.W. Donne, M.F. Montemor, One-step process to form a nickel-based/carbon nanofoam composite supercapacitor electrode using Na_2SO_4 as an eco-friendly electrolyte, RSC Adv. 6 (2016) 15920–15928.

[28] J. Zhang, J. Jiang, H. Li, X.S. Zhao, A high-performance asymmetric supercapacitor fabricated with graphene-based electrodes, Energy Environ. Sci. 4 (2011) 4009–4015.

[29] L. Fornasini, S. Scaravonati, G. Magnani, A. Morenghi, M. Sidoli, D. Bersani, G. Bertoni, L. Aversa, R. Verucchi, M. Riccò, P.P. Lottici, D. Pontiroli, In situ decoration of laser-scribed graphene with TiO2 nanoparticles for scalable high-performance micro-supercapacitors, Carbon N. Y. 176 (2021) 296–306.

[30] V. Augustyn, P. Simon, B. Dunn, Pseudocapacitive oxide materials for high-rate electrochemical energy storage, Energy Environ. Sci. 7 (2014) 1597–1614.

[31] B.E. Conway, Transition from “supercapacitor” to “battery” behavior in electrochemical energy storage, J. Electrochem. Soc. 138 (1991) 1539.

[32] Z. Fan, J. Yan, T. Wei, L. Zhi, G. Ning, T. Li, F. Wei, Asymmetric Supercapacitors Based on Graphene/MnO2 and Activated Carbon Nanofiber Electrodes with High Power and Energy Density, Adv. Funct. Mater. 21 (2011) 2366–2375.

[33] Y. Ding, W. Bai, J. Sun, Y. Wu, M.A. Memon, C. Wang, C. Liu, Y. Huang, J. Geng,

Cellulose Tailored Anatase TiO2 Nanospindles in Three-Dimensional Graphene Composites for High-Performance Supercapacitors, ACS Appl. Mater. Interfaces. 8 (2016) 12165–12175.

[34] Y. Chen, X. Zhang, D. Zhang, P. Yu, Y. Ma, High performance supercapacitors based on reduced graphene oxide in aqueous and ionic liquid electrolytes, Carbon N. Y. 49 (2011) 573–580.

[35] Y. Tian, J. Yan, L. Huang, R. Xue, L. Hao, B. Yi, Effects of single electrodes of Ni (OH) 2 and activated carbon on electrochemical performance of Ni (OH) 2–activated carbon asymmetric supercapacitor, Mater. Chem. Phys. 143 (2014) 1164–1170.

[36] J. Yan, Z. Fan, W. Sun, G. Ning, T. Wei, Q. Zhang, R. Zhang, L. Zhi, F. Wei, Advanced asymmetric supercapacitors based on Ni (OH) 2/graphene and porous graphene electrodes with high energy density, Adv. Funct. Mater. 22 (2012) 2632–2641.

[37] Y. Liu, R. Wang, X. Yan, Synergistic effect between ultra-small nickel hydroxide nanoparticles and reduced graphene oxide sheets for the application in high-performance asymmetric supercapacitor, Sci. Rep. 5 (2015) 11095.

[38] Z. Dai, C. Peng, J.H. Chae, K.C. Ng, G.Z. Chen, Cell voltage versus electrode potential range in aqueous supercapacitors, Sci. Rep. 5 (2015) 9854.

[39] H. Wang, H.S. Casalongue, Y. Liang, H. Dai, Ni (OH) 2 nanoplates grown on graphene as advanced electrochemical pseudocapacitor materials, J. Am. Chem. Soc. 132 (2010) 7472–7477.

[40] M. Gaboardi, R. Tatti, G. Bertoni, G. Magnani, R. Della Pergola, L. Aversa, R. Verucchi, D. Pontiroli, M. Riccò, Platinum carbonyl clusters decomposition on defective graphene surface, Surf. Sci. 691 (2020) 121499.

[41] C. Cavallari, S. Rols, H.E. Fischer, M. Brunelli, M. Gaboardi, G. Magnani, M. Riccò, D. Pontiroli, Neutron scattering study of nickel decorated thermally exfoliated graphite oxide, Int. J. Hydrogen Energy. 44 (2019) 30999–31007.

[42] M. Aramini, G. Magnani, D. Pontiroli, C. Milanese, A. Girella, G. Bertoni, M. Gaboardi, S.

Zacchini, A. Marini, M. Riccò, Nickel addition to optimize the hydrogen storage performance of lithium intercalated fullerides, Mater. Res. Bull. 126 (2020) 110848.

[43] Y. Shao, M. El-Kady, J. Sun, Y. Li, … Q.Z.-C., undefined 2018, Design and mechanisms of asymmetric supercapacitors, ACS Publ. 118 (2018) 9233–9280.

[44] R. Tatti, L. Aversa, R. Verucchi, E. Cavaliere, G. Garberoglio, N.M. Pugno, G. Speranza, S. Taioli, Synthesis of single layer graphene on Cu(111) by C $_{60}$ supersonic molecular beam epitaxy, RSC Adv. 6 (2016) 37982–37993.

[45] S.Q. Liu, H.R. Wen, Ying-Guo, Y.W. Zhu, X.Z. Fu, R. Sun, C.P. Wong, Amorphous Ni(OH)2 encounter with crystalline CuS in hollow spheres: A mesoporous nano-shelled heterostructure for hydrogen evolution electrocatalysis, Nano Energy. 44 (2018) 7–14.

[46] A.E.F. Oliveira, G.B. Braga, C.R.T. Tarley, A.C. Pereira, Thermally reduced graphene oxide: synthesis, studies and characterization, J. Mater. Sci. 53 (2018) 12005–12015.

[47] G. Carturan, G. Cocco, S. Enzo, R. Ganzerla, M. Lenarda, Hexagonal close packed nickel powder: Synthesis, structural characterization and thermal behavior, Mater. Lett. 7 (1988) 47–50.

[48] R.W. Cairns, E. Ott, X-ray studies of the system nickel—oxygen—water. I. Nickelous oxide and hydroxide1, J. Am. Chem. Soc. 55 (1933) 527–533.

[49] A. Mezzi, S. Kaciulis, Surface investigation of carbon films: From diamond to graphite, Surf. Interface Anal. 42 (2010) 1082–1084.

[50] D. Pontiroli, M. Aramini, M. Gaboardi, M. Mazzani, S. Sanna, F. Caracciolo, P. Carretta, C. Cavallari, S. Rols, R. Tatti, L. Aversa, R. Verucchi, M. Riccò, Tracking the hydrogen motion in defective graphene, J. Phys. Chem. C. 118 (2014) 7110–7116.

[51] D. Briggs, G. Beamson, Primary and Secondary Oxygen-Induced C1s Binding Energy Shifts in X-ray Photoelectron Spectroscopy of Polymers, Anal. Chem. 64 (1992) 1729–1736.

[52] D. Briggs, G. Beamson, XPS Studies of the Oxygen 1s and 2s Levels in a Wide Range of Functional Polymers, Anal. Chem. 65 (1993) 1517–1523.

[53] M.C. Biesinger, B.P. Payne, A.P. Grosvenor, L.W.M. Lau, A.R. Gerson, R.S.C. Smart, Resolving surface chemical states in XPS analysis of first row transition metals, oxides and hydroxides: Cr, Mn, Fe, Co and Ni, Appl. Surf. Sci. 257 (2011) 2717–2730.

[54] M.C. Biesinger, B.P. Payne, L.W.M. Lau, A. Gerson, R.S.C. Smart, X-ray photoelectron spectroscopic chemical state Quantification of mixed nickel metal, oxide and hydroxide systems, Surf. Interface Anal. 41 (2009) 324–332.

[55] B.P. Payne, M.C. Biesinger, N.S. McIntyre, The study of polycrystalline nickel metal oxidation by water vapour, J. Electron Spectros. Relat. Phenomena. 175 (2009) 55–65.

[56] A.P. Grosvenor, M.C. Biesinger, R.S.C. Smart, N.S. McIntyre, New interpretations of XPS spectra of nickel metal and oxides, Surf. Sci. 600 (2006) 1771–1779.

[57] G. Wang, Y. Ling, X. Lu, T. Zhai, F. Qian, Y. Tong, Y. Li, A mechanistic study into the catalytic effect of Ni(OH)2 on hematite for photoelectrochemical water oxidation, Nanoscale. 5 (2013) 4129–4133.

[58] R. Afsharipour, S. Dadfarnia, A. Mohammad, H. Shabani, E. Kazemi, A. Pedrini, R. Verucchi, Talanta Fabrication of a sensitive colorimetric nanosensor for determination of cysteine in human serum and urine samples based on magnetic-sulfur , nitrogen graphene quantum dots as a selective platform and Au nanoparticles, Talanta. 226 (2021) 122055.

[59] J. Graetz, C.C. Ahn, H. Ouyang, P. Rez, B. Fultz, White lines and <span class, Phys. Rev. B. 69 (2004) 235103.

[60] M. Chiku, M. Toda, E. Higuchi, H. Inoue, NiO layers grown on a Ni substrate by galvanostatic anodization as a positive electrode material for aqueous hybrid capacitors, J. Power Sources. 286 (2015) 193–196.

[61] D.W. Wang, F. Li, H.M. Cheng, Hierarchical porous nickel oxide and carbon as electrode materials for asymmetric supercapacitor, J. Power Sources. 185 (2008) 1563–1568.

[62] H.M. Yadav, N.C.D. Nath, J. Kim, S.K. Shinde, S. Ramesh, F. Hossain, O. Ibukun, J.J. Lee, Nickel-Graphene nanoplatelet deposited on carbon fiber as binder-free electrode for

electrochemical supercapacitor application, Polymers (Basel). 12 (2020).

[63] J. Woo Lee, Taebin Ahn, Devaraj Soundararajan, J. Myoun Ko, Jong-Duk Kim, Non-aqueous approach to the preparation of reduced graphene oxide /α-Ni(OH) 2 hybrid composites and their high capacitance behavior, Chem. Commun. 47 (2011) 6305–6307.

[64] Hao Jiang, Ting Zhao, Chunzhong Li, Jan Ma, Hierarchical self-assembly of ultrathin nickel hydroxide nanoflakes for high-performance supercapacitors, J. Mater. Chem. 21 (2011) 3818–3823.